Electronic Supplementary Information

Metal Oxide-Zeolite Composites in Transformation of Methanol to Hydrocarbons: Do Iron Oxide and Nickel Oxide Matter?

Joshua Mann[1], Valentin Yu. Doluda[2], Clara Leonard[1], Yaroslav B. Losovyj[1], David Gene Morgan[1], Sergey S. Bukalov[3], Zinaida Shifrina[3], Barry D. Stein[4], Nikolay Cherkasov[5], Evgeny V. Rebrov[2,5], Zachary D. Harms[1], Maren Pink[1], , Esther M. Sulman[2], Lyudmila Bronstein[1, 3, 6]*

[1]Indiana University, Department of Chemistry, Bloomington, IN 47405, USA

[2]Tver State Technical University, Department of Biotechnology and Chemistry, 22 A. Nikitina St, 170026, Tver, Russia

[3]A.N. Nesmeyanov Institute of Organoelement Compounds, Russian Academy of Sciences, 28 Vavilov St., Moscow, 119991 Russia

[4]Indiana University, Department of Biology, Bloomington, IN 47405, USA

[5]School of Engineering, University of Warwick, Coventry, UK CV4 7AL

[6]King Abdulaziz University, Faculty of Science, Department of Physics, Jeddah, Saudi Arabia

---

[*] To whom correspondence should be addressed: lybronst@indiana.edu

Analysis of the reaction products

The reaction gas and liquid mixture was analyzed using an online gas chromatograph (GC). The gas chromatograph (Crystall 2000, Russia) was equipped with a flame-ionization and thermoconductive detectors. The chromatographic analysis was provided under the following conditions: the consumption of gas-carrier (helium): 20 mL/min; gas-carrier pressure: 1.5 kg s/cm^3; duration of the analysis: 40 min; sample volume: 0.25 mL; column (MS-1) length: 100 m; column temperature: 40ºC; heating to 310ºC for 30 minutes and maintaining at this temperature for 5 min. For determination of hydrocarbon composition, the detectors were calibrated using external standards. To determine the exact gas-liquid composition, a gas chromatograph (GC) QP2010 (Shimadzu, Japan), equipped with a quadrupole mass spectrometer (MS) was used with the same column and in the same conditions. The substance identification was provided using the NIST library. Using the GS-MS data, the products were divided into the groups according to the number of carbons in the substances: C_1-C_4, C_5-C_8 and C_9-C_{11} while aromatic hydrocarbons were accounted for separately.

Iron oxide nanoparticle size dependence

For Fe_3O_4-SiO_2-N6, the NPs measure 6.5 nm in diameter. As the Fe precursor loading decreases (Fe_3O_4-SiO_2-N2), the NP size slightly decreases. Even much smaller NPs are obtained at the lowest $Fe(NO_3)_3$ loading (Fe_3O_4-SiO_2-N8) revealing that in this case, the Fe precursor loading is insufficient to form larger NPs. For the silica with 15 nm pores, the NPs are larger, but still much smaller than the pore sizes (Table 1), once again indicating an insufficient amount of the precursor

to form larger NPs. It is noteworthy that iron oxide NPs should not completely fill the pores to allow a contact of reagents with the ZSM-5 surface in the pores. After the ZSM-5 formation, the Fe_3O_4 NP size remains practically unchanged except for the calcined sample when the NP size increases.
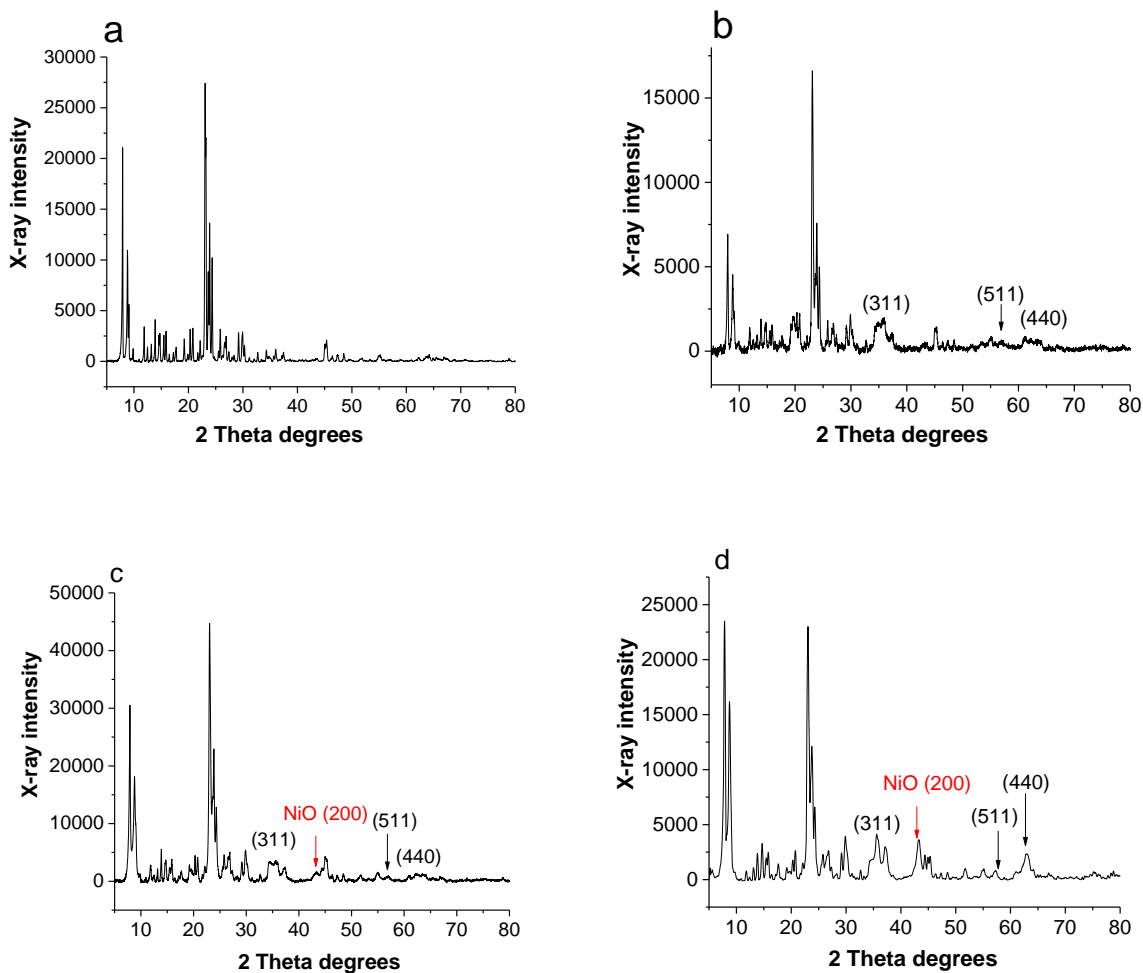
XRD

Figure S1. XRD patterns of 6-ZSM-5 (a), FZ-1 (b), FZ-1-Ni (c), and FZ-1-Ni-calcined (d). The Fe_3O_4 and NiO/Ni_2O_3 reflections becomes stronger after the sample calcination.

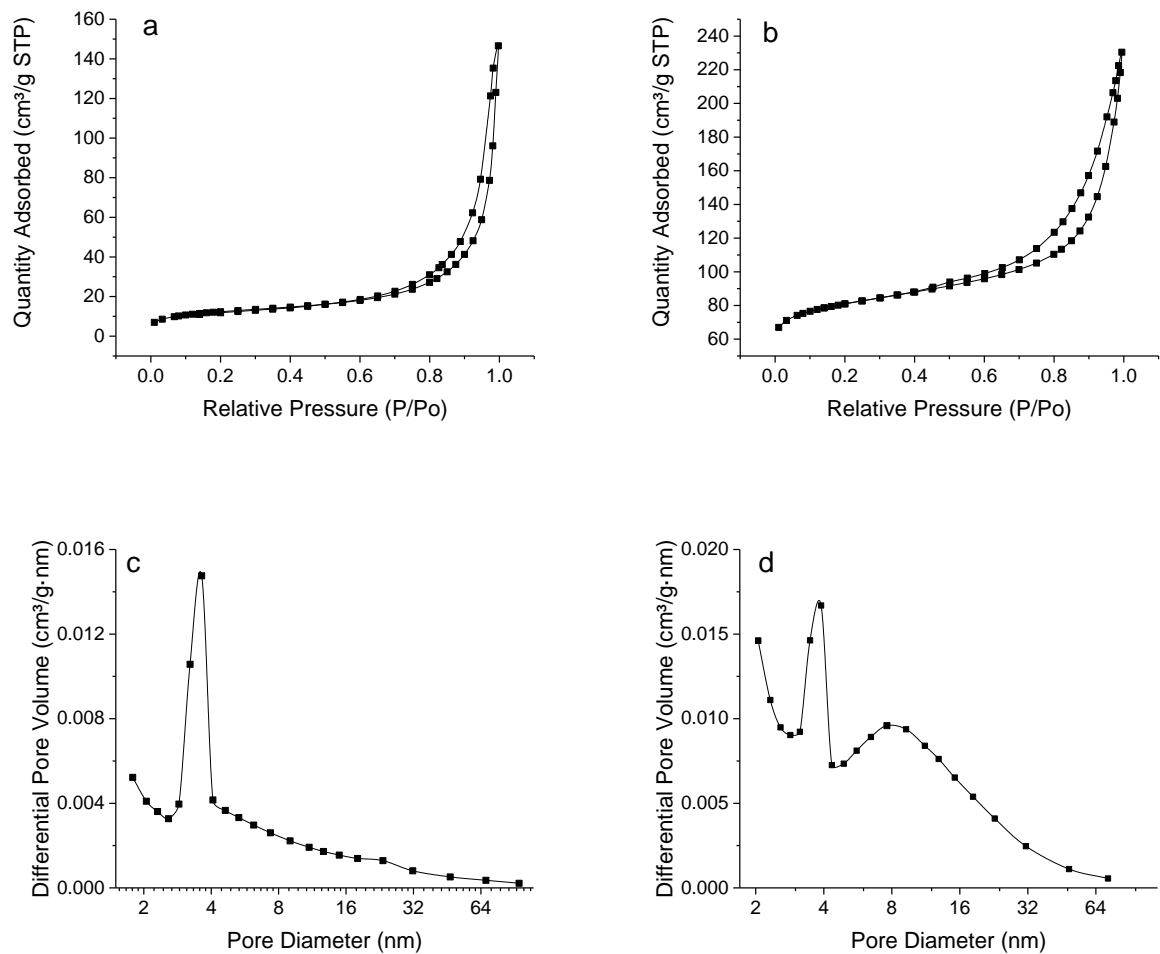**Nitrogen adsorption/desorption isotherms for Fe$_3$O$_4$-ZSM-5**

Figure S2. Nitrogen adsorption-desorption isotherms (a, b) and pore-size distributions (dV/dD) based on BJH desorption data using the Faas correction (c, d) of FZ-1 (a, c) and FZ-1-calcined (b, d).

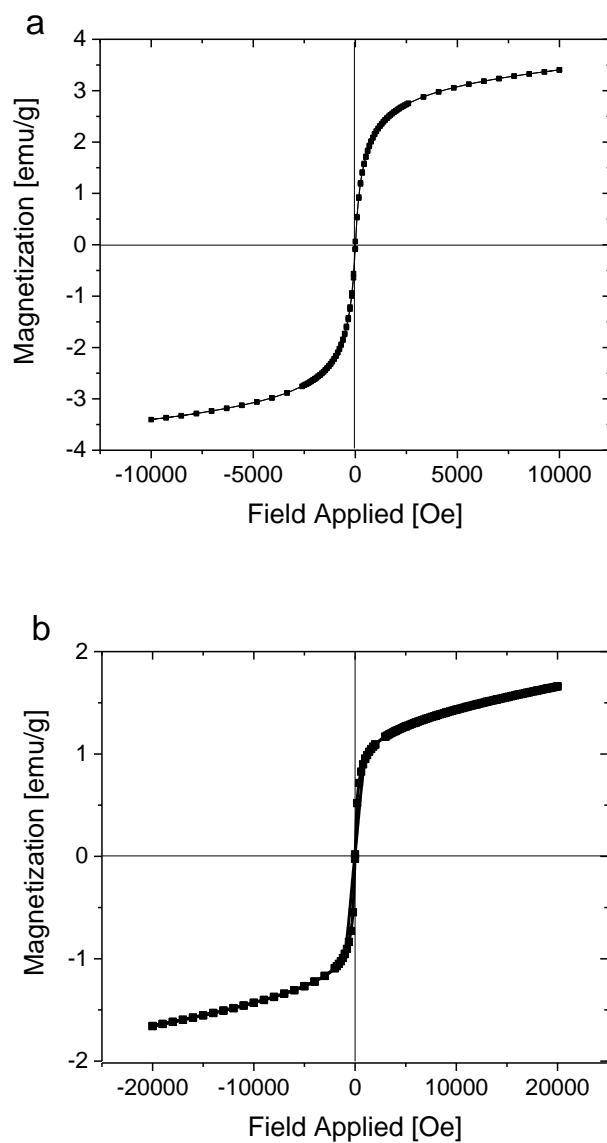**Magnetic properties of Fe₃O₄-ZSM-5**

Figure S3. Isothermal magnetization curves of FZ-1 (a) and FZ-1-calcined (b) at 300K.
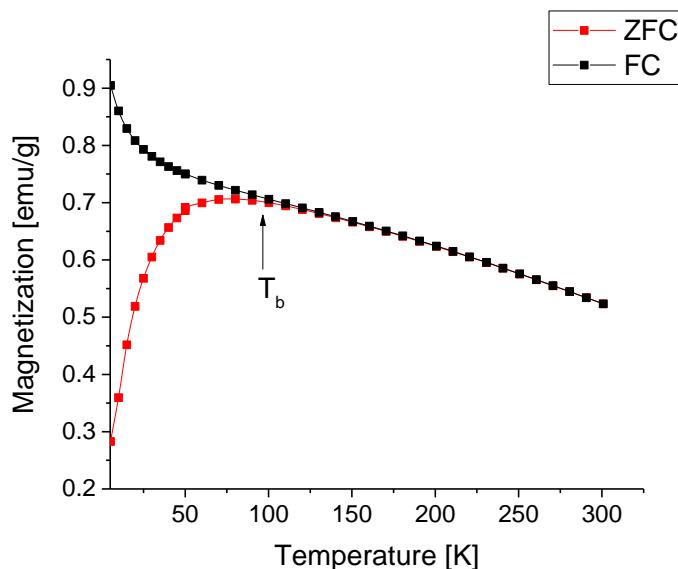
Figure S4. ZFC-FC susceptibility curves as a function of temperature under a magnetic field of 50 Oe for Fe_3O_4-ZSM-5-calcined.

Figure S3 displays isothermal magnetization curves of FZ-1 and FZ-1-calcined, at 300 K. Both curves show no hysteresis which is typical for superparamagnetic NPs. Figure S4 displays zero-field cooling (ZFC) and field cooling (FC) susceptibility curves which allow one to obtain the blocking temperature, T_B, i.e., the point where the two curves merge.[32] The blocking temperature for this sample is about 100 K which is typical for superparamagnetic iron oxide NPs of a comparable size.[33] The low saturation magnetization values, 3.5 emu/g for FZ-1 and 1.8 emu/g for FZ-1-calcined, are due to a small NP size, however, a large number of these NPs allows for fast magnetic separation of the catalyst.

XPS of Fe₃O₄-ZSM-5

Table S1. Parameters of the XPS Fe 2p spectrum for the FZ-1 deconvolution (see Figure 2).

Transition	Position, eV	PosSep, eV	FWHM, eV	%Gauss	%Area	ChiSquared
Fe^{2+} $2p_{3/2}$	710.32	0.00	2.75	90	12.56	
Fe^{2+} $2p_{1/2}$	724.38	14.05	3.2	100	7.18	
Fe^{3+} $2p_{3/2}$	712.32	2.0	3.09	90	25.11	
Fe^{3+} $2p_{1/2}$	726.4	16.07	3.78	100	12.62	1.54
Fe^{2+} $2p_{3/2}$ satellite	714.86	4.54	6.0	96	19.28	
Fe^{2+} $2p_{1/2}$ satellite	728.54	18.22	4.6	83	13.3	
$Fe3^{+}$ $2p_{3/2}$ satellite	721.23	10.9	6.02	100	3.1	
Fe^{3+} $2p_{1/2}$ satellite	734.12	23.8	4.0	84	6.9	

Catalytic properties of the Fe₃O₄-ZSM-5 samples in the MTH process

Table S2. Catalytic performance of the Fe_3O_4-ZSM-5 samples in the MTH process.[a]

Parameter	FZ-2	FZ-3	FZ-4	FZ-5	15-ZSM-5[b]
Methanol conversion rate, g(Methanol)/(g(ZSM-5)×h)	7.3	6.9	6.8	7.0	7.1
DME mixture to hydrocarbons conversion, %	35.6	30.7	28.2	24.8	21.9
including C1-C4	21.1	6.4	5.3	16.8	3.6
including C5-C8	11.4	15.4	18.3	6.8	5.7
including C8-C11	3.1	8.9	5.1	1.2	12.6
DME to aromatics conversion, %	15.7	12.4	22.1	15.2	32.3

[a]Reaction conditions: weight (Al_2O_3): 7.3 g, weight (ZSM-5): 0.1 g, liquid methanol flow rate: 0.02 mL/min, nitrogen flow rate:10 mL/min (STP), temperature: 350 °C, pressure: 5 Bar. [b] The sample 15-ZSM-5 was synthesized in the same conditions as those for Fe_3O_4-ZSM-5 samples but without iron oxide.

The conversion of the DME mixture to hydrocarbons increases over both FZ-4 and FZ-5 catalysts as compared with that over the 15-ZSM-5 catalyst (without iron oxide) prepared from the same silica precursor with a mean pore size of 15 nm. The product distribution over the iron containing NPs changes slightly. The effect becomes more pronounced over the zeolites prepared from the silica precursor with a 6 nm mean pore size.
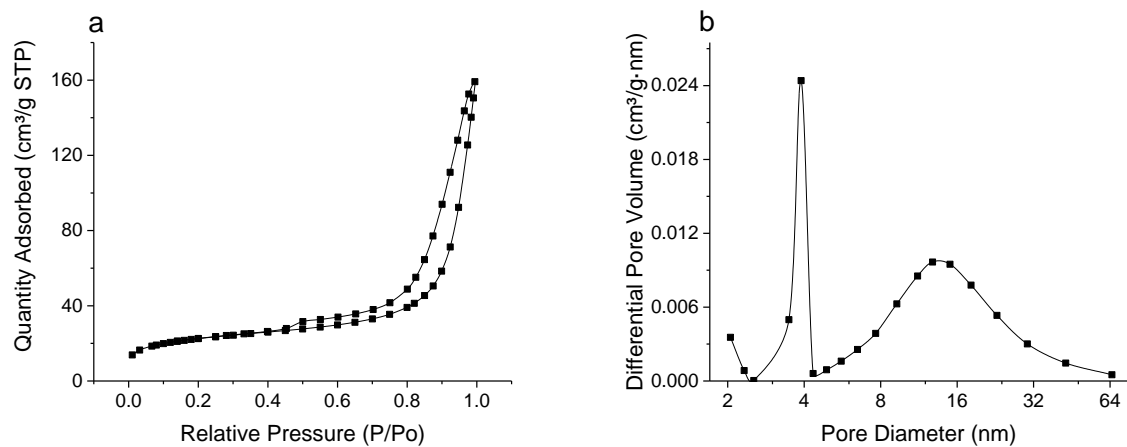
Structure of FZ-1-Ni

Figure S5. Nitrogen adsorption-desorption isotherms (a) and pore-size distribution (dV/dD) based on the BJH desorption data using the Faas correction (b) of FZ-1-Ni.
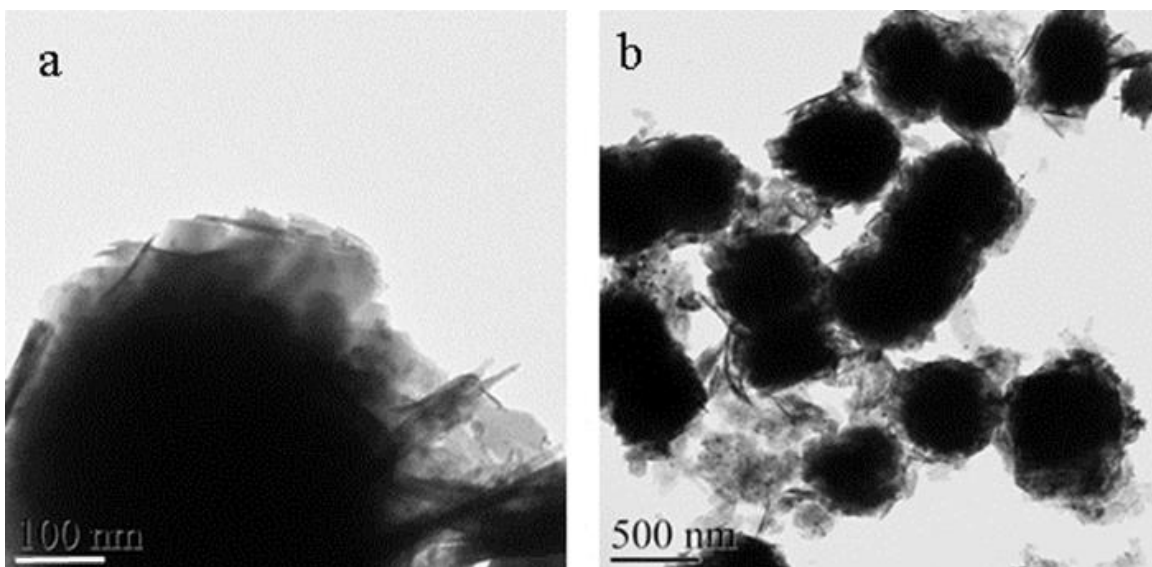

Figure S6. TEM images of FZ-1-Ni (Table 1) at two different magnifications. Scale bars are 100 nm and 500 nm in (a) and (b), respectively.
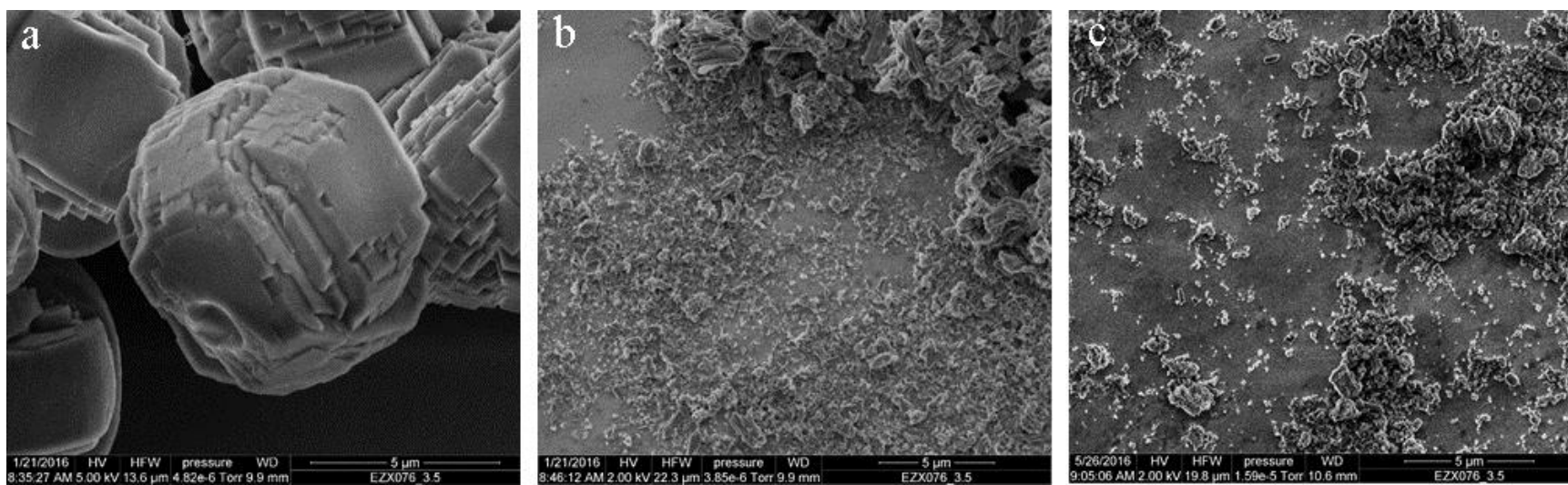
9

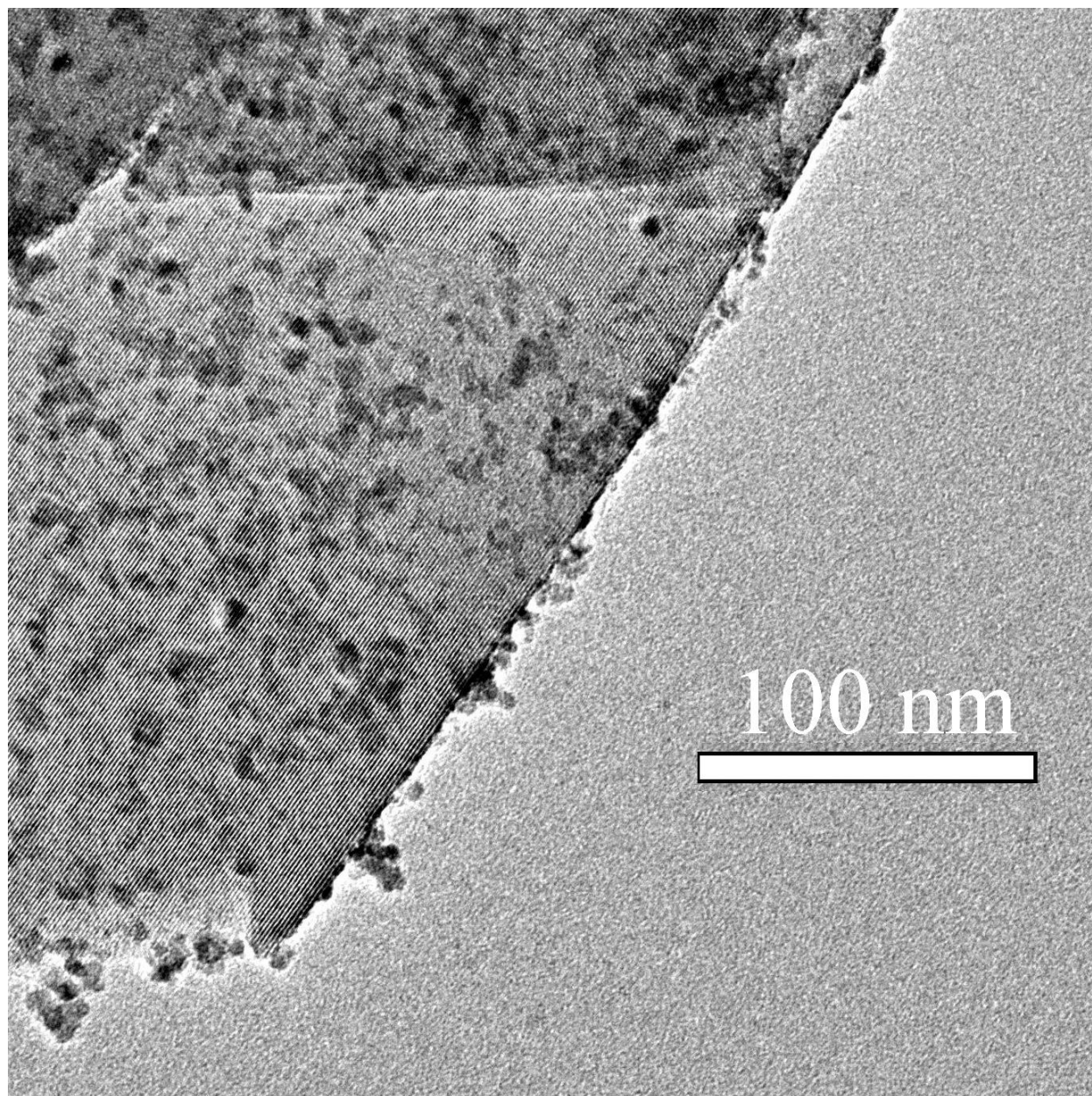Figure S7. SEM images of 6-ZSM-5 (a), FZ-1 (b), and FZ-1-Ni (c). Scale bars are 5 µm.

Figure S8. TEM image of FZ-1-Ni-calcined. It is worth noting that the long exposure of this sample to the electron beam (used to acquire HRTEM) leads to a collapse of the zeolite ordering, while the crystalline structure of metal oxides NPs is preserved. Metal oxide NPs either located in mesopores between the ZSM-5 crystals or embedded in the latter.

Table S3. Elemental composition of Ni-containing Fe_3O_4-ZSM-5 samples from XPS.

Sample notation	XPS content, at.%						Si/Al atomic ratio
	Ni	Si	Al	Fe	O	C	
FZ-1-Ni	5.6	12.4	0.6	3.0	58.0	20.4	21
FZ-1-Ni-calcined	16.1	14.6	0.9	4.7	54.6	9.1	17
FZ-1- calcined-Ni	5.8	18.8	0.7	3.2	59.4	12.1	27

The XPS data show that Ni content is nearly the same (~6 at.%, Table S2) in FZ-1-Ni and FZ-1-calcined-Ni, indicating that the procedure is well reproducible and independent of the material porosity. When the calcination was carried out after nickel oxide incorporation (FZ-1-Ni-calcined), the Ni surface content was much higher: ~16 at.%. This could be attributed to the enrichment of the surface by Ni during calcination. The XPS data also indicate that a considerable fraction of surfactant is removed during calcination. It is noteworthy that the Si/Al ratio decreases from 53 ± 2 (in 6-ZSM-5 and FZ-1) to below 27 after Ni incorporation (FZ-1-Ni, FZ-1-Ni-calcined, and FZ-1-calcined-Ni, Table S3).

Table S4. Parameters of the XPS Ni 2p spectrum for the FZ-1-Ni deconvolution (see Figure 6).

Transition	Position, eV	PosSep, eV	FWHM, eV	%Gauss	%Area	ChiSquared
Ni^{2+} $2p_{3/2}$	854.6	0.00	1.8	90	5.14	
Ni^{3+} $2p_{3/2}$	856.24	1.63	2.9	100	28.58	
satellite	861.9	7.3	5.5	90	32.1	
Ni^{2+} $2p_{1/2}$	872.5	17.9	1.8	100	2.6	1.5
Ni^{3+} $2p_{1/2}$	874.14	19.5	2.9	90	12.3	
satellite	879.9	25.4	5.5	92	19.3	

The surfactant removal is incomplete during calcination in argon at 300 °C for 2 h (conditions of Ni(acac)$_2$ decomposition) resulting in the formation of coke onto less active Si sites. This leads to a partial shielding of the Si sites. Indeed for FZ-1, the Si/Al ratio in the XPS spectra drops from

52 to 36 after calcination. A more pronounced decrease of the Si/Al ratio to 21 is observed in FZ-1-Ni. A preferential coverage of Si vs Al sites by Ni species could explain this observation.

For all three Ni-containing Fe_3O_4-ZSM-5 samples, the HR XPS Fe 2p (Fig. S9) shows solely magnetite NPs even after calcination (12 h in oxygen), indicating the enhanced stability of these particles (Fig. S9).

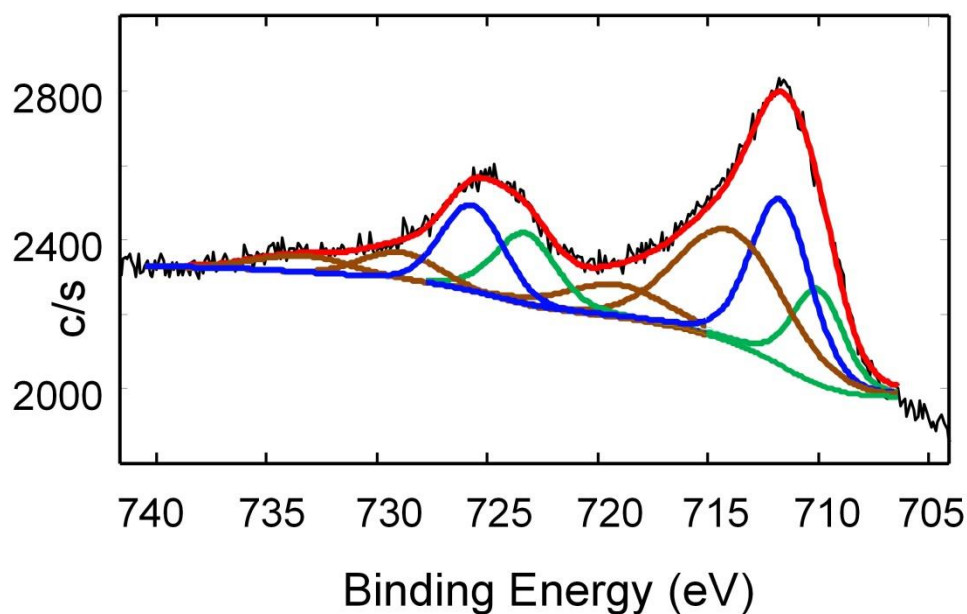Figure S9. HR Fe 2p XPS spectrum of Fe_3O_4-ZSM-5-N2-Ni. The data are shown in black; the generated curve is in red; Fe^{2+} and Fe^{3+} are in green and blue, respectively, and brown shows shake-up curves. See Table S5 for deconvolution parameters.

Table S5. Parameters of the XPS Fe 2p spectrum for FZ-1-Ni deconvolution (Figure S9).

Transition	Position, eV	PosSep, eV	FWHM, eV	%Gauss	%Area	ChiSquared
Fe^{2+} $2p_{3/2}$	710.02	0.00	2.75	90	11.78	
Fe^{2+} $2p_{1/2}$	724.0	13.28	3.3	70	10.6	
Fe^{3+} $2p_{3/2}$	711.72	1.7	3.25	77	23.55	
Fe^{3+} $2p_{1/2}$	725.7	15.68	3.3	89	11.78	1.34
Fe^{2+} $2p_{3/2}$ satellite	714.0	4.0	5.8	90	26.55	
Fe^{2+} $2p_{1/2}$ satellite	729.0	18.98	4.0	100	4.3	
$Fe3^+$ $2p_{3/2}$ satellite	719.1	9.1	5.5	70	10.6	
Fe^{3+} $2p_{1/2}$ satellite	733.4	23.3	5.0	100	3.3	

Product distribution

Table S6. Product distribution in the MTH process.[a]

Parameter	6-ZSM-5	FZ-1	FZ-1-Ni
Methanol conversion rate, g(Met)/(g(Cat)*h)	7.8	7.8	8.2
DME to hydrocarbons conversion, %	13.2	36.7	40.4
including C1-C4	1.2	6.4	7.7
methane	0.7	2.8	3.2
propene	0.3	1.7	2.0
2-methylpropene	0.4	1.9	2.50
including C_5-C_8	2.4	10.3	11.8
2-methylbutene	0.4	1.6	1.9
2-ethylbutene-1	0.6	2.0	2.4
3-methylhexene-1	0.5	1.9	1.7
4-ethylhexene-1	0.3	2.2	2.6
octane	0.4	1.2	1.4
isooctane	0.2	1.4	1.8
including C_9-C_{11}	10.2	21.7	19.8
3-ethyl-4-methylhexene	2.9	5.5	5.7
3,5-diethylheptene	2.5	5.1	5.4
6-methyl-3,5-diethylheptene	2.2	4.3	3.7
3-ethyl-4-methylhexane	2.8	5.9	1.7
3,5-diethylhepthane	0.5	0.1	2.4
6-methyl-3,5-diethylheptane	0.3	0.8	0.9

DME to aromatics conversion	21.8	18.3	22.9
benzene	3.2	2.9	1.2
toluene	2.7	3.1	2.6
2,3,6 - trimethylbenzene	10.2	8.9	17.3
hexamethylbenzene	5.7	3.4	1.8

[a]Reaction conditions are the same as those in Table S1.